Materials Horizons

ROYAL SOCIETY OF CHEMISTRY

COMMUNICATION

View Article Online
View Journal | View Issue

Cite this: *Mater. Horiz.*, 2026, 13, 2479

Received 21st July 2025,
Accepted 5th November 2025

DOI: 10.1039/d5mh01394a

rsc.li/materials-horizons

Oxygen-intercalated Ruddlesden–Popper nickelate: giant resistive switching and emergent multi-electronic phase control

Yufei Yao,†[a] Yanan Zhao, †*[a] Ping Li,†[a] Jie Zou,[a] Zhilu Ye,[a] Xuhui Zhu,[a] Guannan Yang,[a] Shishun Zhao,[a] Guohua Dong,[a] Bin Peng,[a] Qian Li,[b] Zhixin Guo *[a] and Ming Liu *[a]

Rare-earth nickelates exhibit multi-electronic phases that can be dynamically modulated by external stimuli, rendering them promising for neuromorphic computing and sensor applications. However, conventional modulation techniques, such as element doping and ionic liquid gating, typically induce only a single electronic state, thereby weakening the metal–insulator transition and limiting device functionality. Here, we demonstrate that $(NdNiO_3)_n$:NdO samples can sustain multiple electronic states through the intercalation of oxygen ions into Ruddlesden–Popper structures *via* oxygen annealing. This approach achieves a remarkable seven-orders-of-magnitude modulation in resistivity at 250 K and induces non-Fermi liquid behavior with a power-law exponent of 2.75, distinct from the 0.25 exponent observed in perovskite $NdNiO_3$. Theoretical analysis reveals that intercalated oxygen ions mimic the effect of metallic dopants, inducing a ground-state transition from an antiferromagnetic insulator to a ferromagnetic metal. Near the phase transition temperature, the formation of conductive pathways leads to a high-conductivity metallic state. These findings offer crucial insights into oxygen-ion dynamics in Ruddlesden–Popper systems, advancing the design and optimization of strongly correlated oxides for next-generation electronic technologies.

New concepts

Rare-earth nickelates exhibit multi-electronic phases that can be dynamically modulated by external stimuli, rendering them promising for neuromorphic computing and sensor applications. However, conventional modulation techniques, such as element doping and ionic liquid gating, typically induce only a single electronic state, thereby weakening the metal–insulator transition and limiting device functionality. Here, we demonstrate that layered $(NdNiO_3)_n$:NdO heterostructures can sustain multiple electronic states through the intercalation of oxygen ions into Ruddlesden–Popper structures *via* oxygen annealing. This approach achieves a remarkable seven-orders-of-magnitude modulation in resistivity at 250 K and induces non-Fermi liquid behavior with a power-law exponent of 2.75, distinct from the 0.25 exponent observed in perovskite $NdNiO_3$. Theoretical analysis reveals that intercalated oxygen ions mimic the effect of metallic dopants, inducing a ground-state transition from an antiferromagnetic insulator to a ferromagnetic metal. Near the phase transition temperature, the formation of conductive pathways leads to a high-conductivity metallic state. These findings offer crucial insights into oxygen-ion dynamics in Ruddlesden–Popper systems, advancing the design and optimization of strongly correlated oxides for next-generation electronic technologies.

Introduction

Strongly correlated oxides exhibit a range of resistive phenomena, including metal–insulator transition (MIT),[1–5] magnetoresistance,[6–8] and superconductivity,[9–11] offering significant potential for sensing applications. A central challenge in leveraging their full potential lies in achieving stable and reversible multi-state electronic transitions, which are highly sensitive to doping modes and paths.[12–14] Conventional chemical doping strategies have been extensively explored in this regard. For instance, Wang *et al.*[15] doped Ta^{5+} and Ca^{2+} into Co-based perovskite $PrBaCo_2O_{5+\delta}$, reducing its polarization resistance by 18.9%, down to 0.026 Ω cm^2. Abir Nachawaty *et al.*[16] achieved a reversible resistivity change of up to 10^6% in $La_{0.6}Sr_{0.4}MnO_3$/poly(vinylidene fluoride)/Co junctions by driving fluorine-ion migration under applied voltages. Likewise, Zhang *et al.*[17] modulated the resistivity of $SmNiO_3$ films by over four orders of magnitude using salt water-mediated proton exchange. Despite these advances, such chemical doping strategies stabilize only a single electronic state and can even suppress the MIT. Besides, the use of liquid electrolytes may lead to irreversible lattice degradation, ultimately constraining their practical utility.

[a] *State Key Laboratory for Manufacturing Systems Engineering, Collaborative Innovation Center of High-End Manufacturing Equipment, Electronic Materials Research Laboratory, Key Laboratory of the Ministry of Education & International Center for Dielectric Research, School of Electronic Science and Engineering, Xi'an Jiaotong University, Xi'an, 710049, China. E-mail: zhaoyanan1984@xjtu.edu.cn, zxguo08@xjtu.edu.cn, mingliu@xjtu.edu.cn*

[b] *National Synchrotron Radiation Laboratory and School of Nuclear Science and Technology, University of Science and Technology of China, Hefei, Anhui, 230026, China*

† Y. Y., Y. Z. and P. L. are co-first authors.

Researchers[18–20] have proposed a promising alternative approach, utilizing oxygen-ion dynamics to improve the lattice stability and enhance the conductivity. Here, the oxygen-ions could act as a charge transfer channel at the interface due to the low conduction activation energy in oxides. Specifically, La_4NiLiO_8-based cathodes leverage stable oxygen vacancies and preserve the recoverability of the resistance state during cyclic discharge.[21] Introducing oxygen vacancies into metallic state $LaNiO_3$ affects the electronic structure and causes the original Ni^{3+} to change to Ni^{2+} valence, resulting in a metal–insulator transition.[22] Meanwhile, researchers[23–26] have regulated the metal–insulator transition properties and electronic structures of transition metal oxides, utilizing strain engineering. Perovskite $NdNiO_3$ represents a strong metallic state under the in-plane compressive stress caused by lattice mismatch, lowering the metal–insulator transition temperature.[27] Generally, both $LaMnO_3$ and $LaMnO_3$ are antiferromagnetic insulators, while the superlattice heterojunctions show a transition to a ferromagnetic metal state due to the direct static lattice regulation at the heterogeneous interface.[28] Concurrently, nanostructured materials, such as embedded Co–CoN_4@NCNs hybrids,[29] Li-defect-engineered Li_2CoO_3,[30] and cation-tuned Ruddlesden–Popper (R. P.) structures,[31,32] demonstrate dynamic control over electronic states *via* tailored ion channels. These approaches highlight the potential of oxygen-ion engineering and strain engineering to achieve multi-state functionality in correlated oxides, circumventing the limitations of chemical doping.

Here, we report the design and synthesis of $(NdNiO_3)_n$:NdO (n = 1, 2, 3) samples on PMN-PT substrates using pulsed laser deposition, integrating R. P. and perovskite phases. The PMN-PT substrates can be subjected to a larger tensile stress compared to previously reported substrates, and this large stress may induce R. P. homologous series rather than oxygen vacancies in perovskite $NdNiO_3$. Next, intercalated oxygen ions are introduced around the R. P. structures through annealing processes under oxygen conditions, leading to realization of the desired multi-electronic states. Benefiting from this, we achieve a reversible seven-orders-of-magnitude modulation in resistivity at 250 K, demonstrating unprecedented control over the nickelate electronic states. X-ray linear dichroism and density functional theory (DFT) calculations reveal that intercalated oxygen ions stabilize ferromagnetic metallic states, in contrast to the antiferromagnetic insulating ground state of pristine $NdNiO_3$. This transition, accompanied by non-Fermi liquid behavior with a power-law exponent of 2.75, arises from emergent conductive pathways near phase boundaries. These findings position oxygen-intercalated R. P. structures as a promising platform for multistate electronic manipulation, advancing the design of next-generation adaptive correlated oxide devices.

Results and discussion

We synthesized the neodymium nickelate structures on a highly tensile-strained substrate (PMN-PT, ε = 5.3%) (refer to the Methods section for details), including perovskite $NdNiO_3$ and $(NdNiO_3)_n$:NdO (n = 1, 2, 3). Scanning transmission electron microscopy (STEM) reveals a dense formation of R. P. phases in $(NdNiO_3)_n$:NdO films, distinguishing them from the epitaxial perovskite $NdNiO_3$ films on $SrTiO_3$ substrates (Fig. 1a and Fig. S1), while they form lattice defects at the interface to release the larger tensile strain, showing the low HADFF intensity region (Fig. S2). Despite the formation of R. P. structures, these films exhibit excellent crystallinity (EDS, Fig. S3, surface topography, Fig. S4). This structural modulation could provide additional tunability in the electron transport properties. For example, the sheet resistance (R_s) of the R. P. $(NdNiO_3)_n$:NdO films displays a pronounced thermal hysteresis and a sharp metal–insulator (M–I) transition with three orders of magnitude (Fig. 1b), a behavior absent in perovskite $NdNiO_3$.[33] It should be noted that the tensile strain ($\varepsilon < 4\%$) in the growth of perovskite $NdNiO_3$ would introduce oxygen vacancies, leading to off-stoichiometry. Thus, it presents the lack of M–I transition. Next, both the R. P. $(NdNiO_3)_n$:NdO and perovskite $NdNiO_3$ films were treated using *in situ* annealing and post-annealing processes at 673 K (refer to the Methods section for details). Different oxygen annealing methods modulate the resistance states in various ways: *in situ* annealing reduces the oxygen vacancies and relieves the internal stresses in the film growth process, whereas post-annealing enhances the crystal orientation and perovskite phase alignment, improving carrier transport/extraction and suppressing charge recombination at the interface and in the space charge region.[34–36] As shown in Fig. 1c, *in situ* annealing induces a modest resistivity change and an increase in T_{MI} by 27 K. Strikingly, post-annealing alters the temperature-dependent resistivity by seven orders of magnitude above T_{MI} and preserves the M–I transition and multi-electron states. These effects are not observed in perovskite $NdNiO_3$ films under identical annealing conditions (Fig. S5).

The transport properties of the R. P. $(NdNiO_3)_n$:NdO films at different post-annealing temperatures are systematically investigated. As shown in Fig. 2a and b, RS of the R. P. $(NdNiO_3)_n$:NdO films exhibits a strong correlation with the annealing temperature. Upon cooling, the resistance change (ΔR, calculated by insulation resistance $R_{\text{insulation state}}$ minus metallic resistance $R_{\text{metallic state}}$) increases by four orders of magnitude and T_{MI} shifts from 165 K at the initial state to 185 K at a post-annealing condition of 573 K. Furthermore, post-annealing at 673 K induces a ΔR increase of seven orders of magnitude and increases T_{MI} to 244 K, accompanied by the presence of a metallic luster on the film surface (Fig. S6). However, at 773 K, ΔR reduces to two orders of magnitude and T_{MI} decreases to 185 K. Beyond 873 K, the metal–insulator transition of the R. P. $(NdNiO_3)_n$:NdO film vanishes entirely (Fig. S7), likely due to the lattice defects and oxygen desorption disrupting the phase transition.[37–39] To elucidate the underlying transport mechanism, we analyze the resistivity of the perovskite $NdNiO_3$ and R. P. $(NdNiO_3)_n$:NdO films using power laws,[40,41] which can be respectively written as

$$\rho(T) = \rho(0)\exp\left(\frac{A}{T^m}\right), \quad (1)$$

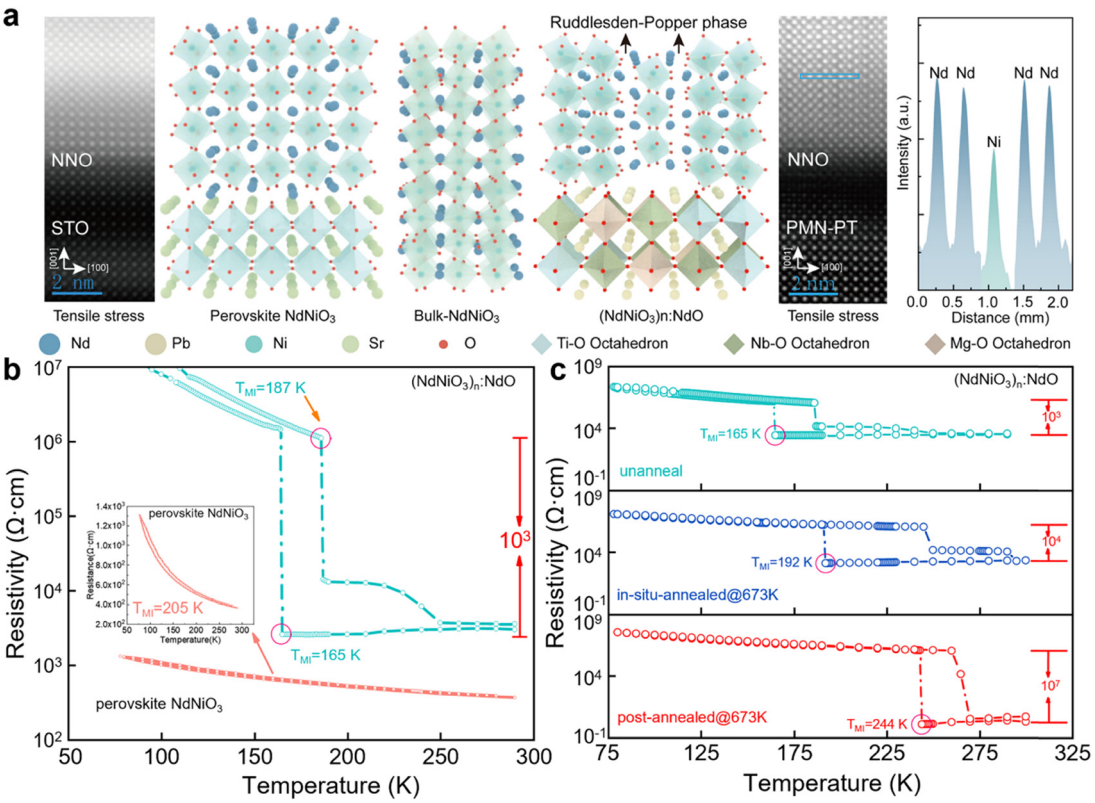

Fig. 1 (a) The change of nanostructure for tensile strain engineering neodymium nickelate, which represents R. P. structures in $(NdNiO_3)_n$:NdO. (b) Resistivity *versus* temperature ($R-T$) curves for R. P. $(NdNiO_3)_n$:NdO films grown on PMN-PT (green line), and perovskite $NdNiO_3$ films grown on $SrTiO_3$ (red line) substrates. Left inset shows the $R-T$ plots of perovskite $NdNiO_3$ films. (c) The changing trend of $R-T$ curves of R. P. $(NdNiO_3)_n$:NdO films, respectively, using post-annealed and *in situ* annealed methods.

$$\rho(T) = \rho(0) + AT^m, \quad (2)$$

where A is a coefficient related to the strength of electron scattering, and m is the power-law exponent. Fig. 2c shows the extracted power-law exponent m for the perovskite $NdNiO_3$ and $(NdNiO_3)_n$:NdO films under three different scenarios (*i.e.*, as-grown, after the *in situ* annealing process, and after the post-annealing process). The resistivity of the perovskite $NdNiO_3$ films exhibits insulating behavior under the three scenarios across the entire temperature range, with power-law exponent m fitted using eqn (1) ranging from 1/4 to 1/2. This behavior suggests that the charge transport in the perovskite $NdNiO_3$ films is primarily dominated by the range hopping mechanism, wherein electrons or holes can jump completely randomly between their localization sites and their nearest neighbor localization sites.[42] By contrast, in all three scenarios, the weak interaction between electrons will significantly affect the electrical properties, and the resistivity often shows a T^2 dependent relationship. The resistivity of the R. P. $(NdNiO_3)_n$:NdO thin films exhibits a typical metallic state above T_{MI}, with the n value fitted using Eqn (2). Particularly, after *in situ* annealing at 673 K, the power-law exponent m of the as-grown R. P. $(NdNiO_3)_n$:NdO film increases from 0.35 to 1.26, signifying a non-Fermi liquid regime associated with reduced oxygen vacancy concentrations, and the limited density of states still exist at the Fermi level, but electrons are localized to a single site. This further confirms that the oxygen vacancies significantly influence the resistivity temperature scaling index, in agreement with prior studies.[40] Additionally, post-annealing at 673 K increases the power-law exponent m of the R. P. $(NdNiO_3)_n$:NdO films to 2.7, indicating that other holes or acceptors enter the valence band through thermal excitation and participate in the conduction process, and suggesting a non-Fermi liquid characteristic. Typically, in strongly correlated Fermi liquids, the resistivity is predominantly governed by the scattering between electrons, following a quadratic temperature (T^2) dependence.[43,44] However, in mixed conductors where both ionic and electronic transport coexist,[45] momentum exchange between charge carriers induces an upward deviation from the T^2 behavior, favoring a higher exponent.[46] Given the observed m value of 2.7 in the post-annealed R. P. $(NdNiO_3)_n$:NdO films, we propose that the transport mechanism is associated with the mixed electronic and ionic conduction, where oxygen ions near the R. P. structures likely contribute to charge transport. Post-annealing treatment enhances the metal–insulator transition temperature to 255 K and increases ΔR to 10^7, significantly exceeding previously reported values.[27,40,46–50]

Generally, the valence state of Ni ions and the concentration of oxygen vacancies are critical factors affecting the electronic

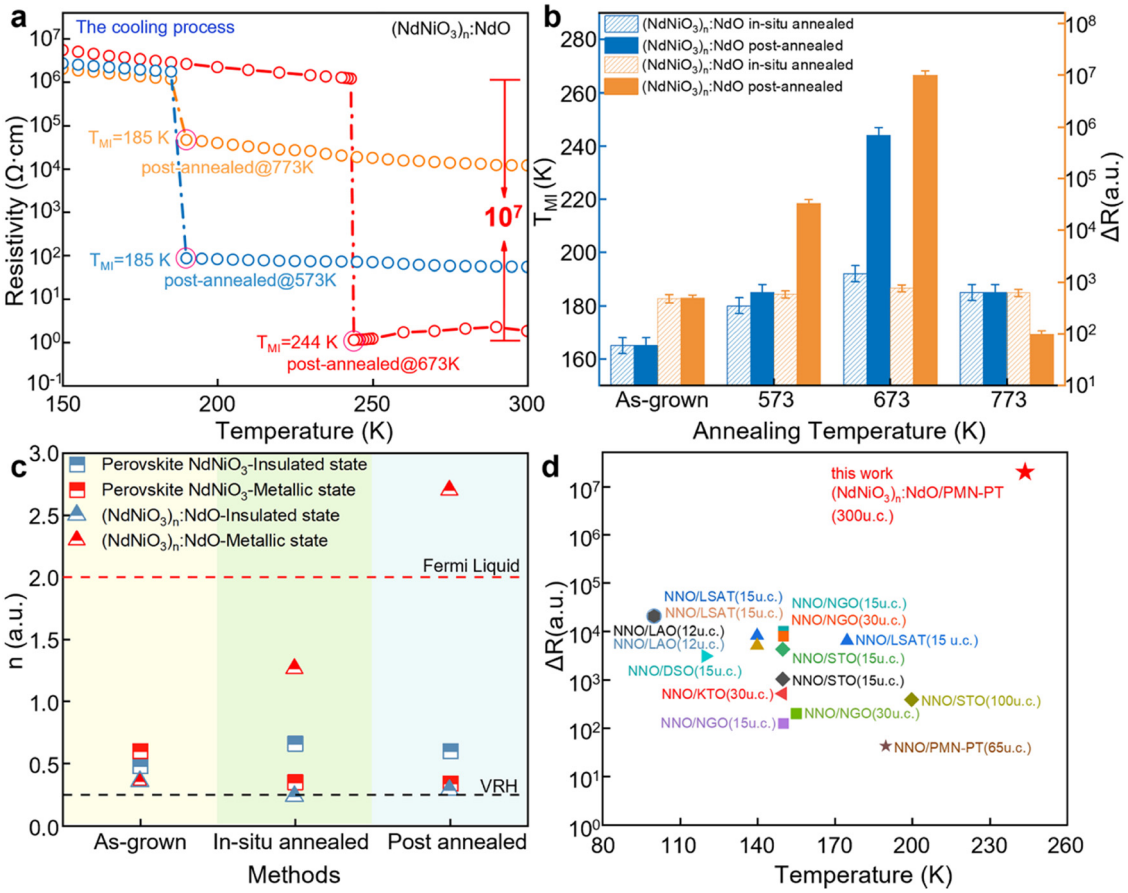

Fig. 2 (a) The changing trend of R–T curves of R. P. $(NdNiO_3)_n$:NdO films in the cooling process, respectively, using post-annealed methods with different temperatures. (b) The metal–insulator transition temperature (T_{MI}) and ΔR as a function of post-annealed temperature, respectively. Here, T_{MI} is extracted from the resistivity data during the cooling-down process, and ΔR is defined as the ratio of the insulator state to the metal state. (c) The power-law exponents (n) of electronic states as a function of different annealed methods. (d) Comparison of this work with previous T_{MI} and ΔR research.

state of strongly correlated nickelates.[51–53] To unveil these effects, XPS was performed on as-grown, *in situ* annealed, and post-annealed R. P. $(NdNiO_3)_n$:NdO films at room temperature (Fig. 3a and b). The O 1s XPS spectrum reveals three distinct binding energy peaks, which, from low to high, correspond to lattice oxygen (~528.5 eV), oxygen vacancies (~530.0 eV), and hydroxyl and oxygen ion (OH^-/O^{2-}) species (~531.7 eV), respectively. The peak area represents the relative concentration of the ligand. Following *in situ* annealing, the oxygen vacancy content is significantly reduced compared to as-grown R. P. $(NdNiO_3)_n$:NdO films, indicating effective suppression of oxygen vacancies. In contrast, post-annealing leads to minimal changes in oxygen vacancy concentration but induces a nearly 70% increase in the contents of hydroxyl and oxygen ions (Table S2). This trend is also observed in perovskite $NdNiO_3$ films, although their electronic states do not exhibit a corresponding response (Fig. S11). To further quantify these observations, the integrated peak area ratio of Ni^{3+}/Ni^{2+} is analyzed using the Ni $2p^{3/2}$ binding energies (~855.3 eV for Ni^{3+} and ~853.5 eV for Ni^{2+}). After *in situ* annealing, the ratio of Ni^{3+}/Ni^{2+} increases from 1.67 in the as-grown films to 4.4, confirming oxygen vacancy annihilation. Post-annealing at 673 K results in a decline to 2.26, yet the ratio remains higher than in as-grown samples. Concurrently, the binding energy of oxygen ions decreases by 0.4 eV under both *in situ* annealing and post-annealing conditions, consistent with the expectations that oxygen ion formation can be enhanced at a temperature of 673 K. Furthermore, post-annealing increases the oxygen ion-to-lattice oxygen ratio to 2.2 in the R. P. $(NdNiO_3)_n$:NdO films, suggesting the emergence of $(NdNiO_3)_n$:$NdO_{1+\delta}$ structure, where δ represents the ratio of oxygen ions intercalated into the films. Although perovskite $NdNiO_3$ films exhibit a similar trend (Fig. S11b and Table S4), their electronic states remain largely unchanged. These results indicate that the electrical transport properties of R. P. $(NdNiO_3)_n$:NdO films are strongly related to the R. P. structures and the interstitial oxygen ions.

To further confirm such conjecture, X-ray absorption spectroscopy is employed to analyze the structure of the R. P. $(NdNiO_3)_n$:NdO films. As depicted in Fig. 3c, the O 1s K-edge spectrum exhibits three distinct peaks: a sharp pre-edge peak at 528 eV, a broad peak at 535 eV, and a doublet peak at around 542 eV, corresponding to Ni 3d–O 2p, Nd 4f–O 2p and Ni 4sp–O 2p hybridization, respectively.[53] Post-annealing leads to a slight reduction in the intensity of the Ni 3d–O 2p pre-edge peak,

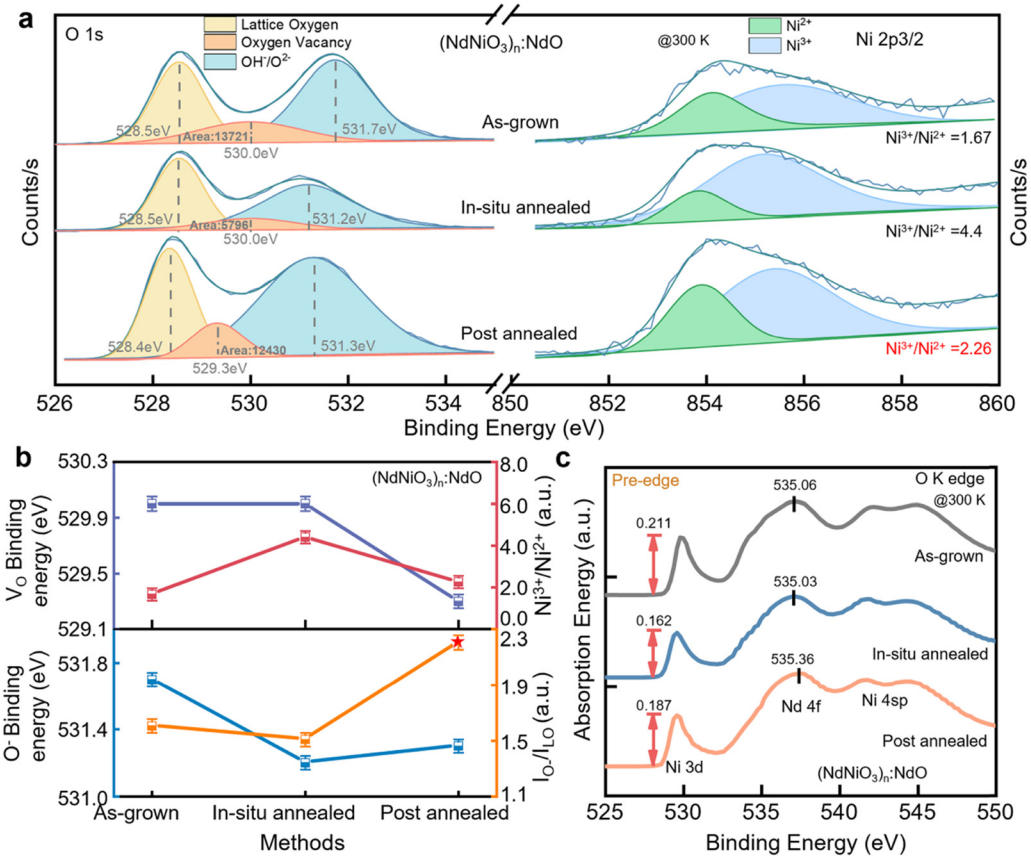

Fig. 3 XPS and XAS spectra of $(NdNiO_3)_n$:NdO films under different annealed methods. (a) O 1s and Ni 2p XPS spectra. (b) Binding energy of oxygen vacancy (V_O) and the intensity ratio of Ni^{3+}/Ni^{2+}. (c) O K edges of XAS spectra.

indicating a diminished formation of O 2p ligand holes and an enhancement in ionicity. Furthermore, the binding energy of Nd 4f–O 2p increases from 535.06 eV to 535.36 eV, accompanied by a 0.3 eV increase in photon energy. These findings confirm the accumulation of oxygen ions around $[NdO]^+$ layers, which impedes the bonding between lattice oxygen and Nd ions, significantly affecting Nd 4f–O 2p hybridization.

By integrating the STEM images in Fig. 1a, we construct a phenomenological model to illustrate the dynamic evolution of the electronic state in post-annealed R. P. $(NdNiO_3)_n$:NdO films (Fig. 4a). This model exhibits a staggered arrangement of $(NdNiO_3)_n$:NdO and $(NdNiO_3)_n$:$NdO_{1+\delta}$ (n = 1, 2, 3) structures, suggesting the presence of multi-electronic states (*e.g.*, semiconductor, insulator or metal), consistent with our experimental findings. To evaluate the substrate effect on the electronic properties of the $(NdNiO_3)_n$:NdO films, which are grown on STO and PMN-PT substrates under different strain conditions, we first calculate the density of states for the perovskite $NdNiO_3$ structure under tensile strains of 2.57% and 5.65%. As shown in Fig. 4(b), the electronic structures near the Fermi level remain largely unchanged under these strains, indicating that the dramatic variation in RS does not originate from the $NdNiO_3$ structure. We then examine the impact of the G-type antiferromagnetic (G-AFM) $(NdNiO_3)$:NdO structure on the electronic transport properties. As shown in Fig. 4(c), the $(NdNiO_3)$:NdO structure exhibits a significantly larger insulating bandgap (1.7 eV) compared to the $NdNiO_3$ structure (0.5 eV).[54] Here, the FM, A-type and G-type AFM states were considered in each structure (Fig. S15). It was found that the G-type AFM state is at least 630 meV per unit cell more stable than other magnetic states in all the three $(NdNiO_3)$:NdO structures (Table S4). In contrast, the ground phases of $(NdNiO_3)_2$: NdO and $(NdNiO_3)_3$: NdO are both metallic (see Fig. S16).[55,56] These features show that the emergence of intrinsic R. P. structures in the form of R. P. $(NdNiO_3)$:NdO structures would lead to a significant increase in RS, consistent with our experimental observation (Fig. 1(c)). Finally, we investigate the electronic properties of $(NdNiO_3)$:NdO intercalated with oxygen ions, *i.e.*, $(NdNiO_3)$:$NdO_{1+\delta}$. The formation energy of $(NdNiO_3)$:$NdO_{1+\delta}$ is calculated over a range of oxygen intercalation concentrations (δ = 0.025–0.0625), yielding results between −5.0 eV and −5.9 eV (Table S5),[57] sufficiently large to facilitate oxygen intercalation. Our findings confirm the experimental observation that the oxygen-intercalated $(NdNiO_3)$:NdO structures can be easily formed through the post-annealing process. Notably, the $(NdNiO_3)$:$NdO_{1+\delta}$ phase exhibits a metallic character with a ferromagnetic (FM) ground state (see Fig. 4(d)), which is calculated by the total energies in different magnetic structures, *i.e.*, FM, A-type and G-type AFM states (Table S6). The oxygen intercalation process not only

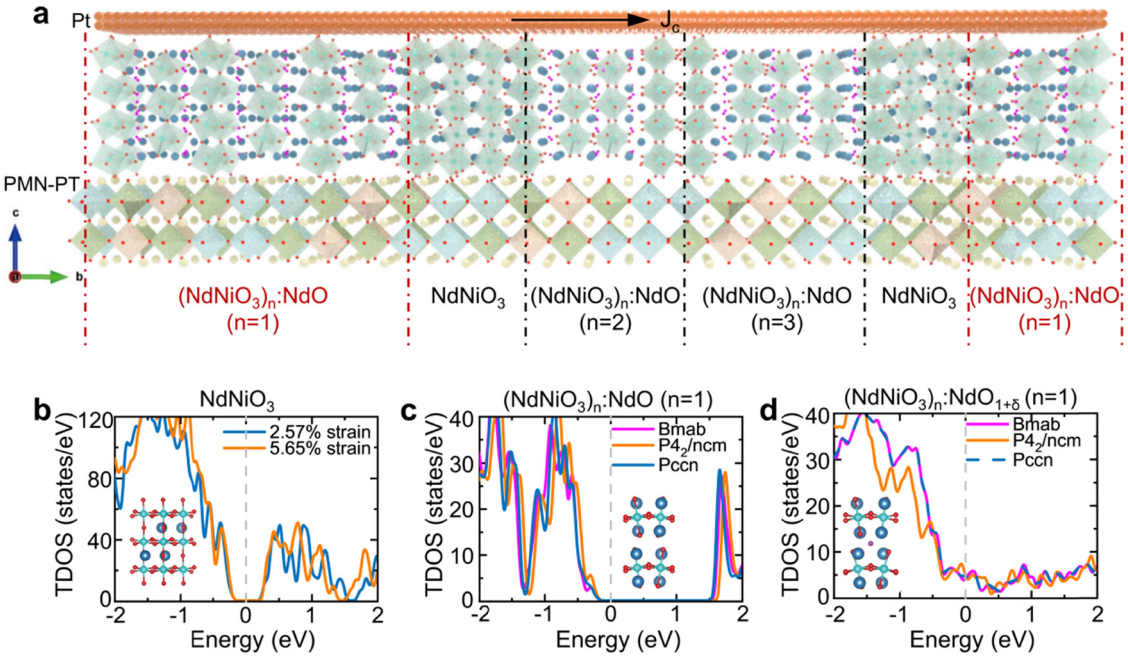

Fig. 4 (a) Schematic diagram of the atomic structure of R. P. $(NdNiO_3)_n$:NdO thin films. The direction of electronic transport is indicated by the black arrow. (b) Total density of states of $NdNiO_3$ with 2.57% and 5.65% tensile strains ($P2_1/n$ structure), respectively. Inset: $NdNiO_3$ structure diagram, where Nd, Ni, and O atoms are depicted by the gray, light blue, and red balls, respectively. (c) Total density of states of R. P. $(NdNiO_3)_n$:NdO (n = 1). Inset: $(NdNiO_3)_n$:NdO (n = 1) structure diagram, where the Nd, Ni, and O atoms are depicted by the gray, light blue, and red balls, respectively. (d) Total density of states of $(NdNiO_3)_n$:$NdO_{1+\delta}$. All lattice structures of $(NdNiO_3)_n$:NdO (n = 1) are considered. Inset: $(NdNiO_3)_n$:$NdO_{1+\delta}$ ($\delta > 0$) structure diagram, where Nd, Ni, lattice O, and intercalated O atoms are depicted by the gray, light blue, red, and magenta balls, respectively.

induces an AFM-FM phase transition but also significantly promotes the insulator-to-metal phase transition, resulting in an extremely low electric resistivity (on the order of several Ω cm above T_{MI}) as observed in our experiment.

Conclusions

In this study, we successfully designed and synthesized Ruddlesden–Popper $(NdNiO_3)_n$:NdO samples, integrating Ruddlesden–Popper and perovskite phases, and achieved a reversible seven-orders-of-magnitude resistivity modulation at the metal–insulator transition through oxygen-ion intercalation. This approach not only reveals non-Fermi liquid behavior driven by mixed electronic and ionic conduction, but also stabilizes ferromagnetic metallic states, which may represent an obvious magnetoresistance effect compared to that of perovskite $NdNiO_3$. These findings highlight the potential of oxygen-intercalated Ruddlesden–Popper structures for multi-state electronic manipulation, advancing the development of next-generation adaptive correlated oxide devices.

Methods

Sample preparation and structure characterization

$NdNiO_3$ (NNO) films were deposited on (001)-oriented $SrTiO_3$ (STO) and (001)-oriented PMN-PT substrates by using a pulsed laser deposition (PLD) method. The deposition temperature of the as-grown sample here was 700 °C, and the growth oxygen pressure was 20 Pa. After deposition, the sample was cooled to room temperature and the oxygen pressure was maintained at 20 Pa. Here, the deposition temperature was kept at 700 °C, and the growth oxygen pressure was kept at 20 Pa. After deposition, the samples were *in situ* annealed and cooled down to room temperature keeping the oxygen pressure at 1×10^4 Pa. In addition, samples were post annealed under an oxygen pressure of 10^4 Pa for 60 min, respectively, at 300 °C, 400 °C, 500 °C, 600 °C, 700 °C and 800 °C in the tubular annealing furnace. The crystalline structures of perovskite and Ruddlesden–Popper $(NdNiO_3)_n$:NdO films were investigated by using high-resolution powder X-ray diffraction (XRD) (HRXRD, Panalytical, Almelo, Holland). The morphology was characterized *via* atomic force microscopy (Bruker, Dimension Icon). Cross-sectional samples for TEM observations were prepared using a focused ion beam technique (FIB, Tescan LYRA 3). Moreover, the microstructure of films was imaged using probe aberration-corrected scanning transmission electron microscopy (Cs-STEM, Themis Z G2 300 kV, FEI). The detector type was HAADF, the camera length was 145 mm, the collection angle range was 39–200 mrad and the electron current was 0.092 nA. In addition, EDS of films were presented using a dual SDD system (dual silicon drift detector), that comprised 2×100 mm^2 SDDs and 1 analyzer.

Transport measurements

The in-plane electric transport properties of samples were investigated using an electromagnet based micro-manipulated probe station (Lakeshore, EMPX-HF) in the temperature range from

78 K to 300 K. The sheet resistances of the samples were obtained by using a linear four point geometry with Pt top electrodes and an Oxford Instruments system and a Keithley 2700 multimeter. During the variable temperature processes, temperature was first decreased from the room temperature (300 K) to the liquid nitrogen temperature (78 K), and then increased from 78 K to 300 K. The test probes used are ZN50R-CVT DC/RF flexible probes, which automatically compensate for the expansion and movement to improve the measurement accuracy in a large temperature range.

X-ray photoelectron spectroscopy (XPS) and absorption spectroscopy (XAS) measurements

The X-ray photoelectron spectroscopy (XPS) measurements were conducted on a Kratos spectrometer (AXIS Ultra DLD) with monochromatic Al Kα radiation ($h\nu$ = 1486.69 eV) and a concentric hemispherical analyzer. The X-ray absorption spectra, including X-ray absorption near-edge structure (XANES) and EXAFS at the Ni and O edge of the samples, were conducted at the ''MCD-A'' beamline and ''XMCD-B'' (Soochow Beamline for Energy Materials) at the National Synchrotron Radiation Laboratory (NSRL) in China. The intensity of X-ray absorption spectra (XAS) was recorded in total electron yield mode. The XAS measurements were carried out in the temperature range of 75 K to 300 K using liquid nitrogen.

Computation methods

We implemented the Vienna *ab initio* simulation package for the first-principles calculations based on the density functional theory (DFT).[58,59] The results are presented for spin arrangements treated at the spin–orbit coupling. The plane-wave basis set with a kinetic energy cutoff of 500 eV was employed. The 8 × 8 × 4 and 8 × 8 × 3 Γ-centered k meshes were adopted for $NdNiO_3$ and Nd_2NiO_4 for the structural optimization, respectively. The geometry optimization was performed until the remaining Hellmann–Feynman forces became less than 0.005 eV $Å^{-1}$ to obtain the final structures. The magnetic ground state and electronic structures were calculated using 2 × 4 × 2 and 10 × 10 × 4 Γ-centered k meshes for $NdNiO_3$ and Nd_2NiO_4, respectively. The exchange correlation energy was described using generalized gradient approximation (GGA) with the Perdew–Burke–Ernzerhof-sol (PBEsol) functional.[60,61] The 4f electrons were frozen in the pseudopotentials. We did not treat explicitly the f electrons in the very low temperature range[62] and they are included in the pseudopotential. Moreover, the GGA+U method was used to describe the strongly correlated 3d orbitals of the Ni atoms.[63] The onsite Coulomb interaction was considered for Ni 3d orbitals by setting effective Hubbard U to 2 eV.

Conflicts of interest

The authors declare no conflict of interest.

Data availability

The data that support the findings of this study are available from the corresponding author upon reasonable request.

The data supporting this article have been included as part of the supplementary information (SI). Supplementary information (SI) is available. See DOI: https://doi.org/10.1039/d5mh01394a.

Acknowledgements

This work was supported by the National Key R&D Program of China (Grant No. 2024YFB3213400), the Natural Science Foundation of China (Grant No. U22A201361 and 623B2082) and the Fundamental Research Funds for the Central Universities. The authors acknowledge the support from the Instrument Analysis Center of Xi'an Jiaotong University and the support from the Users with Excellent Program of Hefei Science Center CAS (No. 2021HSC-UE003). This research used resources of Beamlines XMCD-A and XMCD-B (Soochow Beamline for Energy Materials) at NSRL. Xi'an Jiaotong University's HPC platform and the Hefei Advanced Computing Center of China are acknowledged for generous computational resources.

References

1 G. Catalan, R. M. Bowman and J. M. Gregg, Metal–insulator transitions in $NdNiO_3$ thin films, *Phys. Rev. B: Condens. Matter Mater. Phys.*, 2000, **62**(12), 7892–7900.
2 D. Lee, B. Chung, Y. Shi, G.-Y. Kim, N. Campbell, F. Xue, K. Song, S.-Y. Choi, J. P. Podkaminer, T. H. Kim, P. J. Ryan, J.-W. Kim, T. R. Paudel, J.-H. Kang, J. W. Spinuzzi, D. A. Tenne, E. Y. Tsymbal, M. S. Rzchowski, L. Q. Chen, J. Lee and C. B. Eom, Isostructural metal–insulator transition in VO_2, *Science*, 2018, **362**(6418), 1037–1040.
3 M. Liu, H. Y. Hwang, H. Tao, A. C. Strikwerda, K. Fan, G. R. Keiser, A. J. Sternbach, K. G. West, S. Kittiwatanakul, J. Lu, S. A. Wolf, F. G. Omenetto, X. Zhang, K. A. Nelson and R. D. Averitt, Terahertz-field-induced insulator-to-metal transition in vanadium dioxide metamaterial, *Nature*, 2012, **487**(7407), 345–348.
4 R. Jaramillo, S. D. Ha, D. M. Silevitch and S. Ramanathan, Origins of bad-metal conductivity and the insulator–metal transition in the rare-earth nickelates, *Nat. Phys.*, 2014, **10**(4), 304–307.
5 N. Shukla, A. V. Thathachary, A. Agrawal, H. Paik, A. Aziz, D. G. Schlom, S. K. Gupta, R. Engel-Herbert and S. Datta, A steep-slope transistor based on abrupt electronic phase transition, *Nat. Commun.*, 2015, **6**(1), 7812.
6 A. Chen, Z. Bi, C. F. Tsai, J. Lee, Q. Su, X. Zhang, Q. Jia, J. L. MacManus-Driscoll and H. Wang, Tunable Low-Field Magnetoresistance in $(La_{0.7}Sr_{0.3}MnO_3)_{0.5}$:$(ZnO)_{0.5}$ Self-Assembled Vertically Aligned Nanocomposite Thin Films, *Adv. Funct. Mater.*, 2011, **21**(13), 2423–2429.
7 G. Orfila, D. Sanchez-Manzano, A. Arora, F. Cuellar, S. Ruiz-Gómez, S. Rodriguez-Corvillo, S. López, A. Peralta, S. J. Carreira, F. Gallego, J. Tornos, V. Rouco, J. J. Riquelme,

C. Munuera, F. J. Mompean, M. Garcia-Hernandez, Z. Sefrioui, J. E. Villegas, L. Perez, A. Rivera-Calzada, C. Leon, S. Valencia and J. Santamaria, Large Magnetoresistance of Isolated Domain Walls in $La_{2/3}Sr_{1/3}MnO_3$ Nanowires, *Adv. Mater.*, 2023, **35**, 2211176.

8 M. Bibes, B. Martínez, J. Fontcuberta, V. Trtik, F. Benítez, F. Sánchez and M. Varela, Laser patterned arrays of interfaces in magnetoresistive $La_{2/3}Sr_{1/3}MnO_3$ thin films, *Appl. Phys. Lett.*, 1999, **75**(14), 2120–2122.

9 H. Ji, Y. Liu, Y. Li, X. Ding, Z. Xie, C. Ji, S. Qi, X. Gao, M. Xu, P. Gao, L. Qiao, Y.-F. Yang, G.-M. Zhang and J. Wang, Rotational symmetry breaking in superconducting nickelate $Nd_{0.8}Sr_{0.2}NiO_2$ films, *Nat. Commun.*, 2023, **14**, 7155.

10 Y. Zhang, D. Su, Y. Huang, Z. Shan, H. Sun, M. Huo, K. Ye, J. Zhang, Z. Yang, Y. Xu, Y. Su, R. Li, M. Smidman, M. Wang, L. Jiao and H. Yuan, High-temperature superconductivity with zero resistance and strange-metal behaviour in $La_3Ni_2O_{7-\delta}$, *Nat. Phys.*, 2024, **20**(8), 1269–1273.

11 H. Sun, M. Huo, X. Hu, J. Li, Z. Liu, Y. Han, L. Tang, Z. Mao, P. Yang, B. Wang, J. Cheng, D.-X. Yao, G.-M. Zhang and M. Wang, Signatures of superconductivity near 80 K in a nickelate under high pressure, *Nature*, 2023, **621**(7979), 493–498.

12 E. Morosan, D. Natelson, A. H. Nevidomskyy and Q. Si, Strongly correlated materials, *Adv. Mater.*, 2012, **24**, 4896–4923.

13 T. Li, A. Patz and L. Mouchliadis, Femtosecond switching of magnetism via strongly correlated spin-charge quantum excitations, *Nature*, 2013, **496**, 69–73.

14 A. Georges, L. de' Medici and J. Mravlje, Strong Correlations from Hund's Coupling, *Annu. Rev. Condens. Matter Phys.*, 2013, **4**, 137–178.

15 S. Wang, X. Zhang, Y. Chen, F. Fan, C. Jiang, Y. Xiang, X. Xiao, Y. Fang, A. N. Alodhayb, J. Li, J. Huang, Y. Sun and Z. Chen, Dual-Doping Strategy for Lowering the Thermal Expansion Coefficient and Promoting the Catalytic Activity in Perovskite Cobaltate Air Electrodes for Solid Oxide Cells, *Small*, 2024, 2410672.

16 A. Nachawaty, T. Chen, F. Ibrahim, Y. Wang, Y. Hao, K. Dalla Francesca, P. Tyagi, A. Da Costa, A. Ferri, C. Liu, X. Li, M. Chshiev, S. Migot, L. Badie, W. Jahjah, R. Desfeux, J. C. Le Breton, P. Schieffer, A. Le Pottier, T. Gries, X. Devaux and Y. Lu, Voltage-Driven Fluorine Motion for Novel Organic Spintronic Memristor, *Adv. Mater.*, 2024, **36**, 2401611.

17 Z. Zhang, D. Schwanz, B. Narayanan, M. Kotiuga, J. A. Dura, M. Cherukara, H. Zhou, J. W. Freeland, J. Li, R. Sutarto, F. He, C. Wu, J. Zhu, Y. Sun, K. Ramadoss, S. S. Nonnenmann, N. Yu, R. Comin, K. M. Rabe, S. K. R. S. Sankaranarayanan and S. Ramanathan, Perovskite nickelates as electric-field sensors in salt water, *Nature*, 2017, **553**(7686), 68–72.

18 M. Yashima, T. Tsujiguchi, Y. Sakuda, Y. Yasui, Y. Zhou, K. Fujii, S. Torii, T. Kamiyama and S. J. Skinner, High oxide-ion conductivity through the interstitial oxygen site in $Ba_7Nb_4MoO_{20}$-based hexagonal perovskite related oxides, *Nat. Commun.*, 2021, **12**(1), 556.

19 B. Qiu, M. Zhang, L. Wu, J. Wang, Y. Xia, D. Qian, H. Liu, S. Hy, Y. Chen, K. An, Y. Zhu, Z. Liu and Y. S. Meng, Gas–solid interfacial modification of oxygen activity in layered oxide cathodes for lithium-ion batteries, *Nat. Commun.*, 2016, **7**(1), 12108.

20 Z. A. Feng, F. El Gabaly, X. Ye, Z.-X. Shen and W. C. Chueh, Fast vacancy-mediated oxygen ion incorporation across the ceria–gas electrochemical interface, *Nat. Commun.*, 2014, **5**(1), 4374.

21 L. Wang, G. Liu, R. Wang, X. Wang, L. Wang, Z. Yao, C. Zhan and J. Lu, Regulating Surface Oxygen Activity by Perovskite-Coating-Stabilized Ultrahigh-Nickel Layered Oxide Cathodes, *Adv. Mater.*, 2023, **35**(11), 2209483.

22 L. Wang, S. Dash, L. Chang, L. You, Y. Feng, X. He, K.-j. Jin, Y. Zhou, H. G. Ong, P. Ren, S. Wang, L. Chen and J. Wang, Oxygen Vacancy Induced Room-Temperature Metal-Insulator Transition in Nickelate Films and Its Potential Application in Photovoltaics, *ACS Appl. Mater. Interfaces*, 2016, **8**(15), 9769–9776.

23 D. Meyers, S. Middey, M. Kareev, M. van Veenendaal, E. J. Moon, B. A. Gray, J. Liu, J. W. Freeland and J. Chakhalian, Strain-modulated Mott transition in $EuNiO_3$ ultrathin films, *Phys. Rev. B: Condens. Matter Mater. Phys.*, 2013, **88**(7), 075116.

24 P. D. C. King, H. I. Wei, Y. F. Nie, M. Uchida, C. Adamo, S. Zhu, X. He, I. Božović, D. G. Schlom and K. M. Shen, Atomic-scale control of competing electronic phases in ultrathin $LaNiO_3$, *Nat. Nanotechnol.*, 2014, **9**(6), 443–447.

25 F. Conchon, A. Boulle, R. Guinebretière, E. Dooryhée, J.-L. Hodeau, C. Girardot, S. Pignard, J. Kreisel, F. Weiss, L. Libralesso and T. L. Lee, Investigation of strain relaxation mechanisms and transport properties in epitaxial $SmNiO_3$ films, *J. Appl. Phys.*, 2008, **103**(12), 123501.

26 D. Ferenc Segedin, B. H. Goodge, G. A. Pan, Q. Song, H. LaBollita, M.-C. Jung, H. El-Sherif, S. Doyle, A. Turkiewicz, N. K. Taylor, J. A. Mason, A. T. N'Diaye, H. Paik, I. El Baggari, A. S. Botana, L. F. Kourkoutis, C. M. Brooks and J. A. Mundy, Limits to the strain engineering of layered square-planar nickelate thin films, *Nat. Commun.*, 2023, **14**(1), 1468.

27 J. Liu, M. Kargarian, M. Kareev, B. Gray, P. J. Ryan, A. Cruz, N. Tahir, Y.-D. Chuang, J. Guo, J. M. Rondinelli, J. W. Freeland, G. A. Fiete and J. Chakhalian, Heterointerface engineered electronic and magnetic phases of $NdNiO_3$ thin films, *Nat. Commun.*, 2013, **4**, 2714.

28 A. Bhattacharya, S. J. May, S. G. E. te Velthuis, M. Warusawithana, X. Zhai, B. Jiang, J. M. Zuo, M. R. Fitzsimmons, S. D. Bader and J. N. Eckstein, Metal-Insulator Transition and Its Relation to Magnetic Structure in $LaMnO_3)_{2n}/(SrMnO_3)_n$ Superlattices, *Phys. Rev. Lett.*, 2008, **100**(25), 257203.

29 K. Ding, J. Hu, J. Luo, L. Zhao, W. Jin, Y. Liu, Z. Wu, G. Zou, H. Hou and X. Ji, Robust Electronic Correlation of Co-CoN_4 Hybrid Active Sites for Durable Rechargeable Zn-Air Batteries, *Adv. Funct. Mater.*, 2022, **32**, 2207331.

30 Y. Zhu, Y. Chen, J. Chen, J. Yin, Z. Sun, G. Zeng, X. Wu, L. Chen, X. Yu, H. Luo, Y. Yan, H. Zhang, B. Zhang, X. Kuai, Y. Tang, J. Xu, W. Yin, Y. Qiu, Q. Zhang, Y. Qiao and

S. G. Sun, Lattice Engineering on Li_2CO_3-Based Sacrificial Cathode Prelithiation Agent for Improving the Energy Density of Li-Ion Battery Full-Cell, *Adv. Mater.*, 2023, **36**, 2312159.

31 J. Bak, H. B. Bae, J. Kim, J. Oh and S.-Y. Chung, Formation of Two-Dimensional Homologous Faults and Oxygen Electrocatalytic Activities in a Perovskite Nickelate, *Nano Lett.*, 2017, **17**(5), 3126–3132.

32 G. A. Pan, Q. Song, D. Ferenc Segedin, M.-C. Jung, H. El-Sherif, E. E. Fleck, B. H. Goodge, S. Doyle, D. Córdova Carrizales, A. T. N'Diaye, P. Shafer, H. Paik, L. F. Kourkoutis, I. El Baggari, A. S. Botana, C. M. Brooks and J. A. Mundy, Synthesis and electronic properties of $Nd_{n+1}NiO_{3n+1}$ Ruddlesden-Popper nickelate thin films, *Phys. Rev. Mater.*, 2022, **6**(5), 055003.

33 H. Jeen, W. S. Choi, M. D. Biegalski, C. M. Folkman, I. C. Tung and D. D. Fong, *et al.*, Reversible redox reactions in an epitaxially stabilized $SrCoO_x$ oxygen sponge, *Nat. Mater.*, 2013, **12**, 1057–1063.

34 G. Wu, X. Li, J. Zhou, J. Zhang, X. Zhang, X. Leng, P. Wang, M. Chen, D. Zhang, K. Zhao, S. Liu, H. Zhou and Y. Zhang, Fine Multi-Phase Alignments in 2D Perovskite Solar Cells with Efficiency over 17% via Slow Post-Annealing, *Adv. Mater.*, 2019, **31**, 1903889.

35 R. Tang, S. Chen, Z. H. Zheng, Z. H. Su, J. T. Luo, P. Fan, X. H. Zhang, J. Tang and G. X. Liang, Heterojunction Annealing Enabling Record Open-Circuit Voltage in Antimony Triselenide Solar Cells, *Adv. Mater.*, 2022, **34**(14), 1903889.

36 H. Cai, R. Cao, J. Gao, C. Qian, B. Che, R. Tang, C. Zhu and T. Chen, Interfacial Engineering towards Enhanced Photovoltaic Performance of Sb_2Se_3 Solar Cell, *Adv. Funct. Mater.*, 2022, **32**, 2208243.

37 C.-H. Hsu, X.-P. Geng, W.-Y. Wu, M.-J. Zhao, P.-H. Huang, X.-Y. Zhang, Z.-B. Su, Z.-R. Chen and S.-Y. Lien, Effect of oxygen annealing temperature on properties of spatial atomic layer deposited aluminum-doped zinc oxide films, *Mater. Sci. Semicond. Process.*, 2021, **133**, 105929.

38 G. A. Kimmel and N. G. Petrik, Tetraoxygen on Reduced TiO_2(110): Oxygen Adsorption and Reactions with Bridging Oxygen Vacancies, *Phys. Rev. Lett.*, 2008, **100**, 196102.

39 R. A. Gunasekaran, B. Hellebrand, P. L. Steger and J. D. Pedarnig, Dependence of superconducting transition temperature of $GdBaSrCu_3O_{7-\delta}$ on the annealing temperature, *Mater. Lett.*, 1999, **40**(4), 151–155.

40 Q. Guo, S. Farokhipoor, C. Magén, F. Rivadulla and B. Noheda, Tunable resistivity exponents in the metallic phase of epitaxial nickelates, *Nat. Commun.*, 2020, **11**(1), 2949.

41 K. Ramadoss, N. Mandal, X. Dai, Z. Wan, Y. Zhou and L. Rokhinson, *et al.*, Sign reversal of magnetoresistance in a perovskite nickelate by electron doping, *Phys. Rev. B*, 2016, **94**(23), 235124.

42 B. I. Shklovskii and A. L. Efros, *Electronic Properties of Doped Semiconductors*, Springer-Verlag, 1984.

43 D. Van der Marel, J. L. M. Van Mechelen and I. I. Mazin, Common Fermi-liquid origin ofT2resistivity and superconductivity inn-type $SrTiO_3$, *Phys. Rev. B: Condens. Matter Mater. Phys.*, 2011, **84**, 205111.

44 T. Okuda, K. Nakanishi, S. Miyasaka and Y. Tokura, Large thermoelectric response of metallic perovskites: $Sr_{1-x}La_x$-TiO_3 ($0 < \sim x < \sim 0.1$), *Phys. Rev. B: Condens. Matter Mater. Phys.*, 2001, **63**(11), 113104.

45 X. Lin, B. Fauqué and K. Behnia, Scalable T^2 resistivity in a small single-component Fermi surface, *Science*, 2015, **349**(6251), 945–948.

46 A. Spinelli, M. A. Torija, C. Liu, C. Jan and C. Leighton, Electronic transport in doped $SrTiO_3$: Conduction mechanisms and potential applications, *Phys. Rev. B: Condens. Matter Mater. Phys.*, 2010, **81**(15), 155110.

47 X. Lu, J. Liu, N. Zhang, B. Xie, S. Yang, W. Liu, Z. Jiang, Z. Huang, Y. Yang, J. Miao, W. Li, S. Cho, Z. Liu, Z. Liu and D. Shen, Dimensionality-Controlled Evolution of Charge-Transfer Energy in Digital Nickelates Superlattices, *Adv. Sci.*, 2022, **9**, 2105864.

48 G. Mattoni, P. Zubko, F. Maccherozzi, A. J. H. van der Torren, D. B. Boltje, M. Hadjimichael, N. Manca, S. Catalano, M. Gibert, Y. Liu, J. Aarts, J. M. Triscone, S. S. Dhesi and A. D. Caviglia, Striped nanoscale phase separation at the metal–insulator transition of heteroepitaxial nickelates, *Nat. Commun.*, 2016, **7**(1), 13141.

49 B. Mundet, C. Domínguez, J. Fowlie, M. Gibert, J.-M. Triscone and D. T. L. Alexander, Near-Atomic-Scale Mapping of Electronic Phases in Rare Earth Nickelate Superlattices, *Nano Lett.*, 2021, **21**(6), 2436–2443.

50 Q. Song, S. Doyle, G. A. Pan, I. El Baggari, D. Ferenc Segedin, D. Córdova Carrizales, J. Nordlander, C. Tzschaschel, J. R. Ehrets, Z. Hasan, H. El-Sherif, J. Krishna, C. Hanson, H. LaBollita, A. Bostwick, C. Jozwiak, E. Rotenberg, S.-Y. Xu, A. Lanzara, A. T. N'Diaye, C. A. Heikes, Y. Liu, H. Paik, C. M. Brooks, B. Pamuk, J. T. Heron, P. Shafer, W. D. Ratcliff, A. S. Botana, L. Moreschini and J. A. Mundy, Antiferromagnetic metal phase in an electron-doped rare-earth nickelate, *Nat. Phys.*, 2023, **19**(4), 522–528.

51 C. Hu, X. Wang, T. Yao, T. Gao, J. Han, X. Zhang, Y. Zhang, P. Xu and B. Song, Enhanced Electrocatalytic Oxygen Evolution Activity by Tuning Both the Oxygen Vacancy and Orbital Occupancy of B-Site Metal Cation in $NdNiO_3$, *Adv. Funct. Mater.*, 2019, **29**, 1902449.

52 C. Domínguez, A. B. Georgescu, B. Mundet, Y. Zhang, J. Fowlie, A. Mercy, A. Waelchli, S. Catalano, D. T. L. Alexander, P. Ghosez, A. Georges, A. J. Millis, M. Gibert and J.-M. Triscone, Length scales of interfacial coupling between metal and insulator phases in oxides, *Nat. Mater.*, 2020, **19**(11), 1182–1187.

53 L. Gao, H. Wang, F. Meng, H. Peng, X. Lyu, M. Zhu, Y. Wang, C. Lu, J. Liu, T. Lin, A. Ji, Q. Zhang, L. Gu, P. Yu, S. Meng, Z. Cao and N. Lu, Unveiling Strong Ion–Electron–Lattice Coupling and Electronic Antidoping in Hydrogenated Perovskite Nickelate, *Adv. Mater.*, 2023, **35**, 2300617.

54 T. Arima, Y. Tokura and J. B. Torrance, Variation of optical gaps in perovskite-type 3d transition-metal oxides, *Phys. Rev. B: Condens. Matter Mater. Phys.*, 1993, **48**, 17006–17009.

55 J. Varignon, M. N. Grisolia, J. Iniguez, A. Barthelemy and M. Bibes, Complete phase diagram of rare-earth nickelates from first-principles, *npj Quantum Mater.*, 2017, **2**, 21.

56 D. I. Badrtdinov, A. Hampel and C. E. Dreyer, Interplay between breathing-mode distortions and magnetic order in rare-earth nickelates from ab initio magnetic models, *Phys. Rev. B*, 2021, **104**, 054403.
57 J. Rodruguez-Carvajal, M. T. Fernandez-Diaz, J. L. Martinez, F. Fernandez and R. Saez-Puche, Structural phase-transitions and 3-dimensional magnetic-ordering in the Nd_2NiO_4 oxide, *Europhys. Lett.*, 1990, **11**, 261.
58 G. Kresse and J. Hafner, Ab initio molecular dynamics for liquid metals, *Phys. Rev. B: Condens. Matter Mater. Phys.*, 1993, **47**, 558–561.
59 G. Kresse and D. Joubert, From ultrasoft pseudopotentials to the projector augmented-wave method, *Phys. Rev. B: Condens. Matter Mater. Phys.*, 1999, **59**, 1758–1775.
60 J. P. Perdew, K. Burke and M. Ernzerhof, Generalized gradient approximation made simple, *Phys. Rev. Lett.*, 1996, **77**, 3865–3868.
61 J. P. Perdew, A. Ruzsinszky, G. I. Csonka, O. A. Vydrov, G. E. Scuseria, L. A. Constantin, X. Zhou and K. Burke, Restoring the Density-Gradient Expansion for Exchange in Solids and Surfaces, *Phys. Rev. Lett.*, 2008, **100**, 136406.
62 D. M. Fernandez, J. Alonson, M. Martnez-Lope, M. Casais and J. L. Garca-Munoz, Magnetic structure of the $HoNiO_3$ perovskite, *Phys. Rev. B: Condens. Matter Mater. Phys.*, 2001, **64**, 144417.
63 S. L. Dudarev, G. A. Botton, S. Y. Savrasov, C. J. Humphreys and A. P. Sutton, Electron-energy-loss spectra and the structural stability of nickel oxide: an LSDA+U study, *Phys. Rev. B: Condens. Matter Mater. Phys.*, 1998, **57**, 1505–1509.

